Raman spectroscopy and high spectral resolution luminescence of Ce^{3+} doped $Tb_3Al_5O_{12}$ single crystalline film phosphors grown onto $Gd_3Al_{2.5}Ga_{2.5}O_{12}$ and $Y_3Al_5O_{12}$ substrates

Yurii Syrotych, [*a] *Maciej Rzeczkowski,* [b] *Piotr Radomski,* [b] *Vitaliy Gorbenko,* [a] *Yuriy Zorenko,* [a] *and Tomasz Runka* [*b]

[a]*Faculty of Physics, Chair of Optoelectronic Materials, Kazimierz Wielki University, Powstancow Wielkopolskich 2, 85-090, Bydgoszcz, Poland. E-mail: syr@ukw.edu.pl*

[b]*Institute of Materials Research and Quantum Engineering, Poznan University of Technology, Piotrowo St. 3, 60-965, Poznan, Poland. E-mail: tomasz.runka@put.poznan.pl*

KEYWORDS: Liquid phase epitaxy, Single crystalline films, Ce doping, Raman spectroscopy, High-resolution luminescence

ABSTRACT: We present the results of a study on Raman and high-resolution luminescence spectroscopy of Ce^{3+} - doped $Tb_3Al_5O_{12}$ single crystalline films (SCFs) grown by the liquid phase epitaxy (LPE) method onto $Y_3Al_5O_{12}$ and $Gd_3Al_{2.5}Ga_{2.5}O_{12}$ single crystal (SC) substrates. The Ce^{3+} - doped $Tb_3Al_5O_{12}$ films exhibit a strong Ce^{3+} 5d–4f emission band centred at 560 nm when excited around 488 nm in the vicinity of the 4f–5d absorption band of Ce^{3+} and the 4f–4f absorption bands of Tb^{3+} ions in the visible range. To avoid overlapping with this luminescence, Raman spectra were recorded using a 785 nm excitation wavelength. The lattice mismatch between the $Tb_3Al_5O_{12}$:Ce films and the $Y_3Al_5O_{12}$ and $Gd_3Al_{2.5}Ga_{2.5}O_{12}$ substrates was found to be +0.53% and –1.32%, respectively. The film grown on the $Gd_3Al_{2.5}Ga_{2.5}O_{12}$ substrate exhibits negative and higher residual stress than its counterpart grown onto $Y_3Al_5O_{12}$ substrate. The observed shifts in the positions of the Raman modes for the two epitaxial structures correlate with the differences in lattice constants between the films and their respective substrates. High-resolution luminescence spectra recorded under 488 nm and 785 nm excitation wavelengths reveal 5d–4f and 4f–4f electronic transitions of Ce^{3+} ions and lanthanide trace impurities, respectively.

1. Introduction

In recent decades, aluminum based garnets with the general formula $RE_3Al_5O_{12}$ (RE = Y, Lu, Tb, Gd) have been extensively studied due to their multifunctional applications as laser and magneto-optical devices, scintillation detectors, and phosphors for lighting technologies.[1–4] Among these, cerium - doped $Y_3Al_5O_{12}$ and $Tb_3Al_5O_{12}$ garnets (YAG:Ce and TbAG:Ce) are widely recognized as conventional phosphor converters used in white light-emitting diodes (WLEDs).[5,6] These phosphors function by absorbing blue light from an LED chip and reemitting it as yellow light via Ce^{3+} luminescence, and such combined emission produces white light. The flexibility of the garnet structure, expressed by the general formula $\{RE\}_3[Al]_3(Al)_2O_{12}$, allows

for substitution of cations in the dodecahedral {a}, tetrahedral [b], and octahedral (c) sites. This structural adaptability enables fine-tuning of the composition to optimize the Ce^{3+} luminescence properties for WLED applications.[2,7,8] Traditionally, most commercial WLEDs utilize the volume-casting conversion design, wherein a blue LED is encapsulated with a powder phosphor converter (PC) using organic resins.[9] However, the poor thermal stability of epoxy and silicone resins leads to color degradation and reduced device lifespan under prolonged operation.[10] To address these issues, the planar chip-level conversion strategy has been introduced. In this design, the PC is separated from the LED chip, and ceramic or single-crystal PC, such as YAG:Ce, are employed to enhance performance and thermal stability under blue or near-UV excitation.[11]

Recently, both powder and ceramic forms of TbAG:Ce garnet, grown onto YAG substrates, have emerged as promising candidates for photoconversion applications.[6,12–14] Compared to YAG:Ce, TbAG:Ce exhibits a notably red-shifted Ce^{3+} emission spectrum, attributed to the enhanced crystal field strength at the dodecahedral sites where Ce^{3+} ions are situated. This shift enables the production of WLEDs with lower correlated color temperatures, which is preferable for warm indoor lighting environments. Additionally, efficient energy transfer from the Tb^{3+} sublattice to Ce^{3+} activators improves the overall luminescence efficiency of TbAG:Ce phosphors.[15–19]

Among different phosphor forms, single crystals and single-crystalline films (SCFs) offer significant advantages over ceramics and powders due to their higher thermal conductivity and more homogeneous dopant distribution.[20-27] Moreover, a relatively thick (~500 μm) YAG substrate can absorb a portion of the heat generated by the LED chip, further improving the thermal stability of TbAG:Ce SCF-based phosphor converters compared to their powder counterparts.[25,26,28] However, practical implementation of TbAG:Ce is limited by its incongruent melting behavior, as indicated in the Al_2O_3–Tb_2O_3 phase diagram. This characteristic complicates

the growth of high quality, large-size bulk crystals using the Czochralski (Cz) technique.[29] A potential solution involves partial substitution of Tb^{3+} with Lu^{3+} or Yb^{3+} ions, forming congruently melting solid solutions such as $Tb_{3-x}Lu_xAl_5O_{12}$ or $Tb_{3-x}Yb_xAl_5O_{12}$, which can be grown using micro-pulling-down (μ-PD) and Cz methods.[30,31] Alternatively, SCF of TbAG:Ce in a pure garnet phase can be synthesized via low temperature techniques such as the liquid phase epitaxy (LPE) method.[32,33] LPE is a versatile technique for growing SCFs with controlled thicknesses ranging from a few micrometers to over 200 μm.[34-37]

TbAG:Ce SCFs have been successfully fabricated using a $PbO–B_2O_3$ flux on conventional YAG substrates as well as on $Gd_3Al_{2.5}Ga_{2.5}O_{12}$ (GAGG) substrates, which have lattice constants of 12.011 and 12.233 Å, respectively.[38] Moreover, TbAG:Ce SCFs grown on doped YAG:Ce or GAGG:Ce substrates are being explored as composite scintillators capable of simultaneously detecting different types of ionizing radiation.[39,40]

Typically, SCFs can be grown onto substrates several inches in diameter and subsequently sliced into converters of desired sizes. In addition to the aforementioned optical advantages, SCF-based WLED converters offer superior mechanical strength, chemical resistance, and thermal durability compared to conventional volume-cast phosphor designs. Despite their potential, the application of epitaxially grown film phosphors in pc-WLEDs has been addressed in only a few studies.[20-27] The quantum yield and luminous efficacy of these films, including TbAG:Ce SCFs, have been shown to meet or exceed industrial standards. The critical challenge remains to demonstrate the high crystalline quality of LPE-grown TbAG:Ce SCFs and to validate their advantages over standard powder or ceramic phosphor converters.

This study continues our previous investigations and focuses on the structural and luminescent characterization of Ce^{3+} - doped $Tb_3Al_5O_{12}$ SCFs grown on YAG and GAGG substrates. Advanced

Raman and high-spectral resolution luminescence spectroscopy are employed to assess their suitability as blue-to-yellow converters for high-power WLEDs and scintillation applications as well.

2. Materials and methods

2.1 SCF samples preparation

The two samples under study, in the form of TbAG:Ce SCF/YAG and TbAG:Ce SCF/GAGG epitaxial structures, were grown using the liquid phase epitaxy (LPE) method. The growth was performed from a supercooled melt solution based on a $PbO–B_2O_3$ flux and high-purity (5N) garnet-forming raw materials. The films were deposited onto $Y_3Al_5O_{12}$ (YAG) single crystal (SC) substrate with (110) orientation and a lattice constant of 12.011 Å and $Gd_3Al_{2.5}Ga_{2.5}O_{12}$ (GAGG) single crystal (SC) substrate with (100) orientation and a lattice constant of 12.233 Å (see [38] for details). The lattice mismatch $m = a_{SCF} – a_{sub}/a_{SCF} \times 100\%$ between the TbAG:Ce films and the YAG or GAGG substrates was found to be 0.53% and –1.32%, respectively (see [38] for details).

2.2 Experimental methods

Room temperature (RT) unpolarized Raman spectra of $Tb_3Al_5O_{12}:Ce^{3+}$ grown onto $Gd_3Al_{2.5}Ga_{2.5}O_{12}$ SC (TbAG:Ce/GAGG) and $Tb_3Al_5O_{12}:Ce^{3+}$ grown onto $Y_3Al_5O_{12}$ SC (TbAG:Ce/YAG) were obtained using a Renishaw inVia Raman microscope equipped with a thermoelectrically (TE)-cooled CCD detector. A semiconductor laser with an excitation wavelength of 785 nm was used with aim to avoid overlapping with a strong luminescence of Ce^{3+} centered at 560 nm. Prior to Raman spectra measurements, the samples of TbAG:Ce/GAGG and TbAG:Ce/YAG were specially prepared. The samples were broken along selected direction, which allow to obtain a cross section through the TbAG:Ce SCFs and GAGG SC or YAG SC substrate. **The cross-section of the sample was not polished before spectroscopic measurements**.

For an excitation wavelength of 785 nm and an objective with a magnification of ×150 and numerical aperture (NA) of 0.95, the spatial resolution is approximately 1 μm. The power of the laser beam focused on the sample was kept below 20 mW and constantly controlled to maintain consistent measurement conditions. The spectra were recorded in a 100-900 cm^{-1} region with a spectral resolution better than 2 cm^{-1}. Prior to data acquisition, the spectrometer was calibrated using a reference crystalline silicon sample as an external standard. The spectra processing was performed in WiRE 3.4 software.

High spectral resolution luminescence (HSRL) spectra of 30 μm thick TbAG:Ce SCF grown onto GAGG SC substrate and 21 μm thick TbAG:Ce SCF grown onto YAG SC substrate were recorded at room temperature (RT) using the same Renishaw inVia Raman microscope. A 488 nm excitation line of the Ar^+ ion laser and the aforementioned 785 nm line of the semiconductor laser were used. The applied laser powers for mentioned excitation lines were 0.05 mW and 20 mW, respectively. The spectral resolution was exactly the same as for the measurements of Raman spectra, i.e., better than 2 cm^{-1}. The spatial resolution for wavelengths of 488 nm and 785 nm (NA = 0.95) was roughly 0.6 μm and 1 μm, respectively.

3. Results and discussion

3.1 Raman spectroscopy characterization

TbAG:Ce crystallizes in the form of a garnet crystal structure, which belongs to the cubic lattice with its symmetry described by the space group no. 230 - $Ia\bar{3}d$ (O_h^{10}).[41] In the $Tb_3Al_2(AlO_4)_3$ garnet structure, each oxygen atom is shared among two dodecahedra, one tetrahedron, and one octahedron. Tb^{3+} and Al^{3+} cations are coordinated by O^{2-} anions in three different ways: Tb^{3+} cations are surrounded in an 8-fold (dodecahedral) configuration, some Al^{3+} cations are in 6-fold (octahedral) coordination, and the remaining Al^{3+} cations are in 4-fold (tetrahedral) coordination.

The Ce^{3+} ion, as an activator, typically replaces the Tb^{3+} cation during Ce^{3+} intentional doping due to the similar ionic sizes and valence states of both cations.[42] As a result, the local environment around the Ce^{3+} ion in the garnet structure is commonly described by a CeO_8 moiety.[43] For the O_h^{10} structure of TbAG, a primitive cell contains 4 formula units (Z_p=4) resulting in 80 atoms in a unit cell. Group theory analysis for the $Ia\bar{3}d$ space group predicts the reducible representation near the center of Brillouin zone (q ~ 0) as follows:

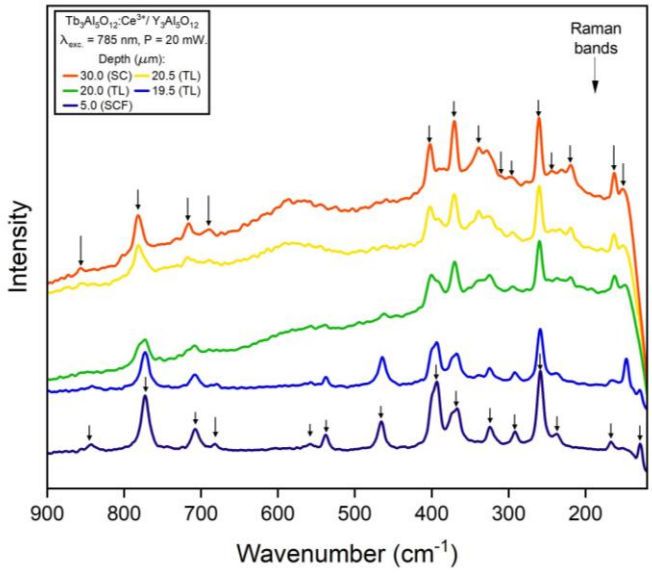
$$\Gamma = 3A_{1g} + 5A_{2g} + 8E_g + 14F_{1g} + 14F_{2g} + 5A_{1u} + 5A_{2u} + 10E_u + 18F_{1u} + 16F_{2u}$$

where only 25 of 240 listed normal modes of vibrations are Raman-active ($3A_{1g} + 8E_g + 14F_{2g}$), 17 F_{1u} modes are present in infrared absorption spectra, 55 modes are optically silent and one triply degenerated F_{1u} is an acoustic mode.[44-46]

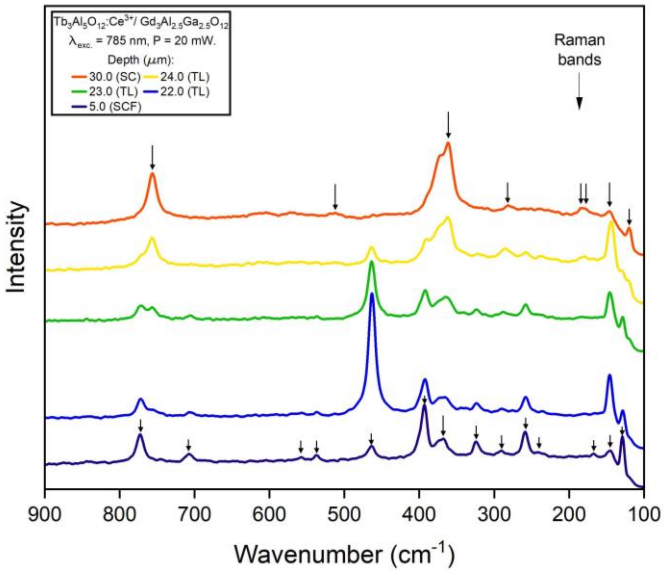
The distinctive feature of intentionally doped or co-doped with Ce^{3+} ions garnet matrices is a prominent and strong photoluminescence (PL) occurring at 560 nm, associated with the 5d-4f electron transition of the Ce^{3+} ion after excitation with light from the visible region at 460 nm. For this reason, aforementioned semiconductor laser with a wavelength of 785 nm was chosen to record the Raman spectra. Unpolarized Raman scattering spectra were registered at RT. The spectra were obtained starting from the edge of the film to 40 μm deep into the sample cross-section for GAGG substrate and to 30 μm deep into the sample cross-section for YAG substrate. The experimental spectra revealed fewer Raman modes than the 25 theoretically predicted by group theory analysis, mainly because of three important factors: some modes might be too weak, preventing us from observing them, accidental degeneracies may cause some modes to overlap, making them indistinguishable and also some Raman modes might be mixing with 4f-4f electronic transitions of unintentional trace lanthanides.[47-52]

For the purpose of analysis, five representative Raman spectra were selected for the

TbAG:Ce/GAGG and the TbAG:Ce/YAG samples. The obtained spectra are shown in Figures 1a and 1b.



(a)



(b)

Figure 1. RT unpolarized Raman spectra of the $Tb_3Al_5O_{12}$:Ce SCF grown onto $Y_3Al_5O_{12}$ (a) and $Gd_3Al_{2.5}Ga_{2.5}O_{12}$ (b) SC substrates.

Measurements were performed along the cross-section, moving from the film edge towards the

substrate, using an excitation wavelength of 785 nm. The solid arrows indicate the observed Raman bands corresponding to the normal vibrations for $Tb_3Al_5O_{12}$, $Gd_3Al_{2.5}Ga_{2.5}O_{12}$ or $Y_3Al_5O_{12}$ garnets. The depth of the cross-section of the sample, along which Raman spectra were measured, increases from bottom to top in both figures (Figs. 1a, 1b) starting from the TbAG:Ce SCF edge. The modes observed near the sample edges are associated with the $Tb_3Al_5O_{12}$:Ce SCF's. Those situated at the greatest depth of the cross-section belong to the $Gd_3Al_{2.5}Ga_{2.5}O_{12}$ SC and $Y_3Al_5O_{12}$ SC substrates. The spectra from the middle positions reflect the changes caused by passing through the transition layer (TL), which acts as a buffer layer between the epitaxial layer and the substrate. The existence of TL has been confirmed by our recent research.[44,47,53-55] Analyzing the measurements taken along the cross-section of the samples, we are able to estimate that the transition layer spans the distance from 22 μm to 24 μm for TbAG:Ce/GAGG and from 19.5 to 20.5 μm for TbAG:Ce/YAG, with corresponding thicknesses of about 2 μm and 1 μm. This means that the resulting SCFs thickness is at 22 and 19.5 μm for TbAG:Ce/GAGG and TbAG:Ce/YAG, respectively. That is significantly different from the results obtained by the weighing method, for which the estimated SCF thicknesses were on the order of 30.0 and 21.0 μm. The most possible reason for that is the local nature of the Raman spectra measurement.

A typical approach found in the literature is the separation of the first-order Raman spectra of garnets in the range 100-900 cm^{-1}, into distinct spectral regions.[44,47,50-53,56,57] The first region is known as the low-wavenumber region, located in the range of 100-500 cm^{-1}. The region that occurs in the range of 500-600 cm^{-1}, is called the intermediate-wavenumber region. The high-wavenumber region is the last separated region, covering the range of wavenumbers up to 900 cm^{-1}. This classification allows us to analyze the observed Raman modes by associating them with the vibrations of isolated tetrahedral AlO_4 molecular unit within the structure of $A_3B_2(BO_4)_3$ garnet

compounds. The low-wavenumber region, between 100 and 500 cm^{-1} is associated with the lattice modes like translational motion of RE^{3+} ions and AlO_4 tetrahedra, librational motion of AlO_4 units and also antisymmetric stretching vibration ν_3 of AlO_4 groups.[44,47,50,53,57-59] Modes occuring in the intermediate-wavenumber region between 500 and 600 cm^{-1} are attributed to ν_2 quadruple vibrations of AlO_4 tetrahedra. The high-wavenumber region, i.e., from 600 to 900 cm^{-1}, includes the modes assigned to the breathing ν_1 and deformation ν_4 internal vibrations associated with AlO_4 groups.[51,53,57-59] The proposed assignment of Raman modes recorded for $Tb_3Al_5O_{12}$:Ce SCFs and also $Gd_3Al_{2.5}Ga_{2.5}O_{12}$ and $Y_3Al_5O_{12}$ SC substrates is presented in Tables 1-4. Due to the lack of previous literature data on Raman spectra for $Gd_3Al_{2.5}Ga_{2.5}O_{12}$ garnet, to evaluate the symmetry and the assignment of observed Raman modes, we used the information from the previously studied garnet crystals of similar chemical composition i.e. $Gd_3Ga_3Al_2O_{12}$ and $Gd_3Ga_5O_{12}$ (GGG).[60-62]

Table 1. Experimentally observed Raman bands of $Tb_3Al_5O_{12}$:Ce grown onto $Gd_3Al_{2.5}Ga_{2.5}O_{12}$ SC substrate with their symmetry types and their assignment in relation to the previously published literature.

Wavenumber (cm^{-1})	Literature data				Symmetry type & Assignment	
TbAG:Ce/GAGG	TbAG [44]	TbAG [48]	TbAG [49]	TbAG [52]		
128	129	130	-	-	F_{2g}	
145	-	-	139	-	E_g	
167	166	167	167	-	F_{2g}	
240	239	238	-	238	F_{2g}	
258	259	263	259	263	F_{2g}	RE^{3+} Translations;
291	292	293	293	293	F_{2g}	Translations +
324	324	326	-	326	E_g	Librations +
368	366	369	372	369	A_{1g}	ν_3 (AlO_4)
394	393	396	396	395	F_{2g}	
464	-	-	-	-	E_g/ F_{2g}	
537	538	-	-	537	F_{2g}	ν_2 (AlO_4)
558	559	558	560	558	A_{1g}	
708	708	-	-	707	F_{2g}	$\nu_1 + \nu_4$ (AlO_4)
772	773	774	-	774	A_{1g}	

Table 2. Experimentally observed Raman bands of $Tb_3Al_5O_{12}$:Ce grown onto $Y_3Al_5O_{12}$ SC substrate with their symmetry types and their assignment in relation to the previously published literature.

Wavenumber (cm^{-1})		Literature data			Symmetry type & Assignment	
TbAG:Ce/YAG	TbAG [44]	TbAG [48]	TbAG [49]	TbAG [52]		
128	129	130	-	-	F_{2g}	
167	166	167	167	-	F_{2g}	
237	239	238	-	238	F_{2g}	
258	259	263	259	263	F_{2g}	RE^{3+} Translations;
291	292	293	293	293	F_{2g}	Translations +
324	324	326	-	326	E_g	Librations +
368	366	369	372	369	A_{1g}	ν_3 (AlO_4)
394	393	396	396	395	F_{2g}	
464	-	-	-	-	E_g/ F_{2g}	
537	538	-	-	537	F_{2g}	ν_2 (AlO_4)
558	559	558	560	558	A_{1g}	
681	682	686	690	686	F_{2g}	$\nu_1 + \nu_4$ (AlO_4)
707	708	-	-	707	F_{2g}	
772	773	774	-	774	A_{1g}	
845	843	850	848	850	F_{2g}	

Table 3. Experimentally observed Raman bands of $Gd_3Al_{2.5}Ga_{2.5}O_{12}$ single crystal substrate with their symmetry types and our proposed assignment.

Wavenumber (cm^{-1})	Literature data		Symmetry type & Assignment	
GAGG SC substrate	$Gd_3Ga_3Al_2O_{12}$ [62]	$Gd_3Ga_5O_{12}$ [56]		
119	118	-	F_{2g}	
145	-	-	E_g	RE^{3+} Translations;
177	180	170.3	F_{2g}	Translations +
184	-	180.3	F_{2g}	Librations +
281	281	274.0	F_{2g}	ν_3 (Al, Ga)O_4
361	362	354.5	A_{1g} - F_{2g}	
512	510	507.3	F_{2g}	ν_2 (Al, Ga)O_4
756	758	-	A_{1g}	ν_1 (Al, Ga)O_4

Table 4. Experimentally observed Raman bands of $Y_3Al_5O_{12}$ SC substrate with their symmetry types and their assignment in relation to the previously published literature.

Wavenumber (cm^{-1})	Literature data				Symmetry type & Assignment	
YAG SC substrate	[47]	[50]	[51]	[59]		
151	-	144	145	145	F_{2g}	
162	162	162	163	163	E_g	RE^{3+} Translations;
219	219	218	220	220	F_{2g}	Translations +
244	-	243	243	243	F_{2g}	Librations +
260	264	259	261	261	F_{2g}	ν_3 (AlO_4)

296	291	296	295	295	F_{2g}	
310	310	310	310	310	E_g	
339	339	340	340	340	E_g	
370	371	373	370	370	A_{1g}	
402	402	403	402	402	Eg	
690	-	690	691	691	F_{2g}	
717	717	719	718	718	F_{2g}	$\nu_1 + \nu_4$ (AlO_4)
782	784	783	783	783	A_{1g}	
856	-	857	857	857	F_{2g}	

The unpolarized Raman spectra of $Tb_3Al_5O_{12}$:Ce SCFs grown onto GAGG and YAG SC substrates (Figs. 1a, 1b) were recorded at room temperature using a near-infrared semiconductor laser with an excitation wavelength of 785 nm. The laser power was consistently set at 20 mW for each measurement. For the $Tb_3Al_5O_{12}$:Ce SCF grown onto a $Gd_3Al_{2.5}Ga_{2.5}O_{12}$ SC substrate, 14 of the 25 Raman modes predicted by group theory analysis were experimentally observed at: 128, 145, 167, 240, 258, 291, 324, 368, 394, 464, 537, 558, 708 and 772 cm^{-1} respectively, and for the same SCF grown onto a $Y_3Al_5O_{12}$ SC substrate, the presence of fifteen Raman modes at: 128, 167, 237, 258, 291, 324, 368, 394, 464, 537, 558, 681, 707, 772, 845 cm^{-1} was experimentally recorded. The recorded spectra for TbAG:Ce SCFs contain only Raman modes, which confirms the stability of the epitaxial growth process resulting in the high quality of the obtained TbAG:Ce SCFs. Because of the missing literature data on Raman spectroscopy of $Gd_3Al_{2.5}Ga_{2.5}O_{12}$, eight observed Raman bands were assigned to a particular type of symmetry by using the available literature data for structurally and chemically similar garnets: $Gd_3Ga_5O_{12}$ (GGG) and $Gd_3Ga_3Al_2O_{12}$.[56,62] The corresponding band positions for these structures were found, and then the symmetry type and assignment of the observed Raman bands in the GAGG structure were determined by comparison.

In Figure 1b, the evolution of Raman spectra for TbAG:Ce/GAGG illustrates that over a comparable wavenumber range, the observed Raman modes are redshifted e.g. 128 → 119 cm^{-1} (F_{2g}). This shift is related to the transition towards the GAGG SC region. Due to the higher lattice constant of GAGG (12.233 Å) compared to TbAG:Ce (12.073 Å),[60,61] the Raman bands are moved to lower wavenumber values. The above mentioned vibration, as well as the Raman bands at 145, 177 and 184 cm^{-1} were assigned to the translational motions of Gd^{3+} ions. It is worth noting that the position of modes assigned to translational motions should depend on the mass of RE cations, however, in this case, the mass of Gd^{3+} and Tb^{3+} is comparable. Thus, in this case shift of the position of translational motions of RE^{3+} cations depends on atomic distances RE – O. Two sharp bands at: 281 and 361 cm^{-1} were assigned to translational, librational and internal antisymmetric stretching vibrations ν_3 of (Al, Ga)O_4 tetrahedra. Presumably, the observed band at 361 cm^{-1} is the result of the overlapping of two Raman bands with A_{1g} and F_{2g} symmetry types, respectively. The observed low-intensity mode at 512 cm^{-1} and the high-intensity mode at 756 cm^{-1} were assigned to quadruple ν_2 and breathing ν_1 vibrations of (Al, Ga)O_4 tetrahedra, respectively. Because of the higher lattice constant of GGG (12.385 Å) with respect to GAGG (12.233 Å),[56,61] the Raman band positions for this structure will be shifted towards lower wavenumber values compared to the observed GAGG bands. The consequence of the differences in lattice constants and the available literature data for $Gd_3Ga_3Al_2O_{12}$ and $Gd_3Ga_5O_{12}$ garnet structures allowed us to determine the symmetry types for all of the eight observed Raman bands in $Gd_3Al_{2.5}Ga_{2.5}O_{12}$ structure (see Tab. 3). The recorded spectra from the surfaces of the GAGG and YAG SC substrates (Figs. 1a, 1b) are the result of superposition of Raman modes and also very weak luminescence bands associated with an unintentional presence of lanthanide (Ln) elements and the electronic transitions occurring in them, especially for YAG SC. In the context of Raman scattering, luminescence is a very

undesirable process. Its intensity is several orders of magnitude greater than the intensity of Raman scattering, hence even a marginal amount of unintentional Ln^{3+} ion impurities can cause strong luminescence bands visible in the recorded spectra, which often make Raman modes impossible to observe. Raman spectra of the YAG substrate (e.g. 30 μm) show several sharp and broad bands.

An increase in background intensity in range between 150 and 400 cm^{-1} and a gently broader band at approximately 580 cm^{-1} are attributed to the electronic transitions of marginal amounts of Ln^{3+} ions present as unintentional dopants. A similar but much less intensive effect was observed for the Raman spectra of the GAGG SC substrate (e.g. 30 μm), where a few broader bands at 570 and 605 cm^{-1} were observed. The appearance of Ln^{3+} ions could be explained by the fact that, rare earth element oxides such as Y_2O_3, Gd_2O_3 and Ce_2O_3 used in the process of crystal growth, always contain trace amounts of impurities from other REs. Nonetheless, after the analysis of Raman spectra from the substrates, we can conclude that the YAG SC substrate was much more contaminated by unintentional lanthanide impurities than the GAGG SC substrate, or the 785 nm line used does not excite the electronic transitions of unintentional Ln^{3+} impurities as much in the GAGG structure. The recorded Raman spectra for the $Gd_3Al_{2.5}Ga_{2.5}O_{12}$ SC substrate contains eight sharp bands at: 119, 145, 177, 184, 281, 361, 512 and 756 cm^{-1} which are Raman modes and for the $Y_3Al_5O_{12}$ SC substrate, fourteen Raman modes were experimentally observed at 151, 162, 219, 244, 260, 296, 310, 339, 370, 402, 690, 717, 782 and 856 cm^{-1} (see Tabs's. 3, 4).

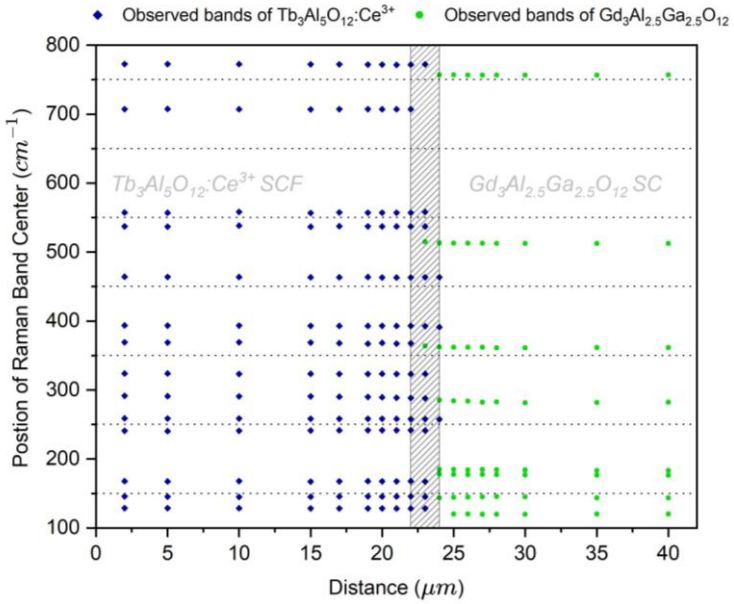
To properly interpret the above mentioned results, it is necessary to introduce the concept of the SCF–substrate interface and the transition layer (TL). According to [54], the interface thickness between the TbAG SCF and the YAG substrate is very small, on the order of 5–6 nm (approximately 5–6 lattice constants). While we did not conduct a similar detailed analysis for the TbAG:Ce/GAGG structure, it is expected that its interface thickness is only slightly larger than

that of the TbAG:Ce/YAG structure. Therefore, it can be assumed that the chemical composition of the interface range represents a solid solution: $(Tb_{1-x}Gd_x)_3Al_{2.5}Ga_{2.5}O_{12}$ for the TbAG:Ce/GAGG structure and $(Tb_{1-x}Y_x)_3Al_5O_{12}$ for the TbAG:Ce/YAG structure, with the parameter x varying from 0 to 1 across the transition from the SCF to the substrate. Meanwhile, the TL is situated in close proximity to the SCF–substrate interface, where a gradual compositional change occurs. Figures 1a and 1b, which display the Raman spectra of TbAG:Ce SCFs grown onto GAGG and YAG SC substrates, clearly confirm the presence of this TL near the SCF–substrate interface. The TL is identified at depths of approximately 22–24 μm in the TbAG:Ce/GAGG structure and 19.5–20.5 μm in the TbAG:Ce/YAG structure. Within the TL zone, we observe a superposition of the Raman spectra of the SCFs and their respective substrates in this region for both samples. This likely indicates a partial or even full relaxation of mechanical strain in the TL, leading to variations in cation–anion distances, and corresponding modifications in the Raman spectra of TbAG:Ce/YAG and TbAG:Ce/GAGG structures.

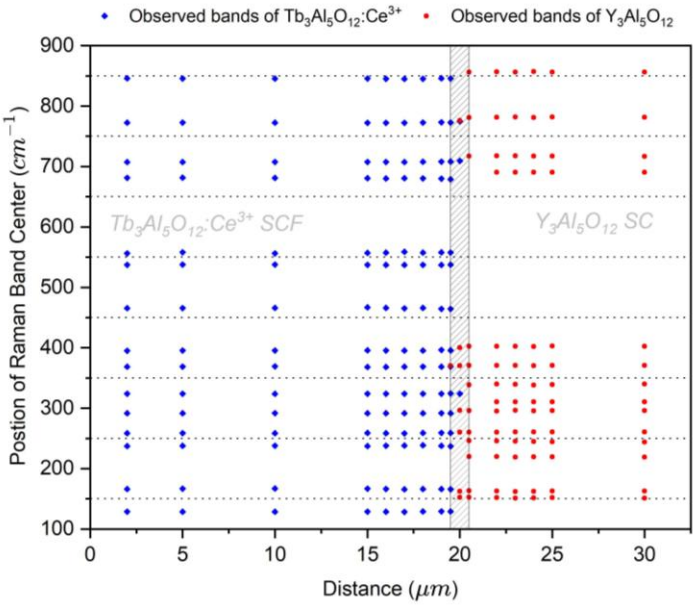
To investigate and characterize the evolution of the observed Raman modes, during the transition from SCF through TL to the substrate, peak center positions (PCPs) were determined as a function of the probing distance along the cross section for both samples. The obtained results are shown in Figures 2a and 2b. The peak center positions assigned to the Raman bands change with probing distance, as illustrated in Figures 2a and 2b. For the TbAG:Ce SCF grown onto GAGG SC (Fig. 2a) one Raman band appears at the same wavenumber, i.e. 145 cm^{-1}. This band is attributed to the translational motions of RE^{3+} ions. No change in band position, can be explained by the similar atomic masses ($m_{Tb^{3+}}$= 158.93 a.m.u. ~ $m_{Gd^{3+}}$ = 157.25 a.m.u.) and ionic radii ($R_{Tb^{3+}}$ = 1.040 Å ~ $R_{Gd^{3+}}$ = 1.053 Å) of Tb^{3+} and Gd^{3+} ions resulting in the same wavenumber value.

Going from the TbAG:Ce SCF layer to the GAGG SC substrate, there is a noticeable shift in the

bands towards the lower wavenumber values. It is an anticipated consequence related to a higher lattice constant of the GAGG substrate (12.233 Å) in comparison with that of the epitaxial TbAG:Ce SCF (12.073 Å),[60,61] as the higher interatomic distances cause the red shift of Raman modes.



(a)



(b)

Figure 2. Peak center positions (PCPs) of observed Raman modes as a function of the probing distance from the SCF edge for the $Tb_3Al_5O_{12}$:Ce/$Gd_3Al_{2.5}Ga_{2.5}O_{12}$ (a) and $Tb_3Al_5O_{12}$:Ce/$Y_3Al_5O_{12}$ (b) structures. Estimated transition layer position and thickness was illustrated by dashed rectangle.

For the same TbAG:Ce SCF grown onto YAG SC substrate, the shifts of Raman bands laying in comparable ranges of wavenumbers are also related to the change in a lattice constant when going from the TbAG:Ce SCF layer to the YAG SC substrate. In the range of low-wavenumbers as well as high-wavenumbers, we observed shifts of bands with different symmetry types such as E_g i.e. 324 → 339 cm^{-1}, F_{2g} i.e. 707 → 717 cm^{-1} and A_{1g} i.e. 772 → 782 cm^{-1} when moving from the epitaxial TbAG:Ce SCF to the YAG SC substrate. Bands with these symmetry types are related to the vibrations of the AlO_4 units of the garnet structure. Compared to GAGG SC, YAG SC has a smaller lattice constant (12.011 Å) than TbAG:Ce SCF (12.073 Å). Thus, it is sure that as a consequence of a smaller bond lengths in the AlO_4 tetrahedral subgroups, the force constants will increase and then the individual Raman bands will blue shift. The above-mentioned results are consistent with those obtained by Dewo et al. by the analysis of the TbAG:Mn SCF grown onto the YAG SC substrate.[44]

For both epitaxial TbAG:Ce SCFs grown onto GAGG SC and YAG SC substrates, a Raman band was observed at 464 cm^{-1}, which was not reported in the literature yet. This band can probably be assigned to deformation vibration of AlO_4 tetrahedra of E_g or F_{2g} symmetry. In Fig. 3, we observe that as we move further into the cross-section of the sample, the above mentioned band becomes significantly more intense, reaching a maximum value of its intensity near the region of the transition layer (22.0 μm), and as we leave the TL, we observe a rapid decrease in the intensity of this vibration and its complete extinction in the region of the GAGG substrate. For

the same TbAG:Ce SCF grown onto a YAG SC substrate, we do not observe an ”uplift” effect of the 464 cm^{-1} band as we approach the TL.

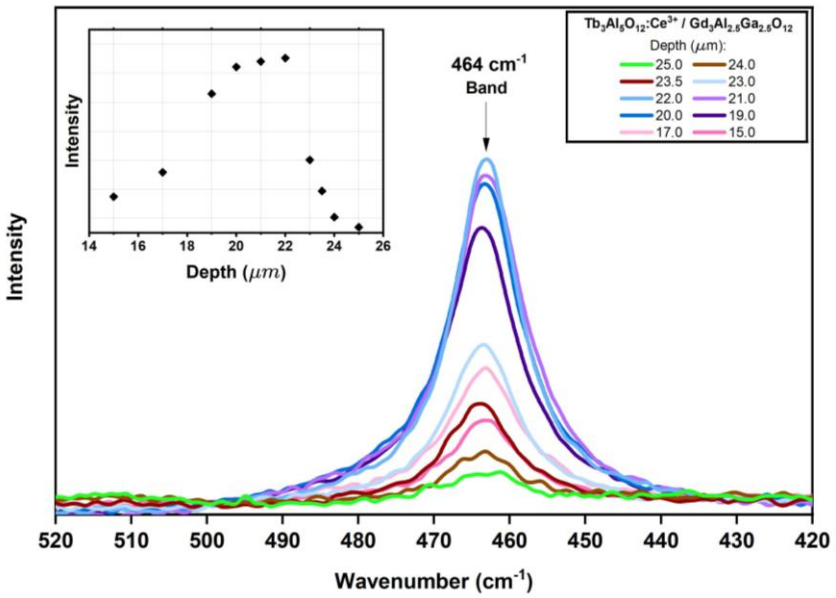


Figure 3. The fluctuations in intensity of observed 464 cm^{-1} band with the change in depth along the cross-section of the $Tb_3Al_5O_{12}$:Ce/$Gd_3Al_{2.5}Ga_{2.5}O_{12}$ structure. The change in the intensity vs depth is shown in the inset.

The transition layer might be a region of emerging mechanical stresses which can affect the vibrational and optical properties of such composite materials. Gradual changes in the PCPs, FWHMs and integral intensities of Raman bands in the vicinity of the TL region may indicate the propagation of these stresses deep into the epitaxial layer and substrate area. For epitaxially grown SCF onto SC substrates, a lattice misfit parameter m along certain crystallographic direction is defined as:

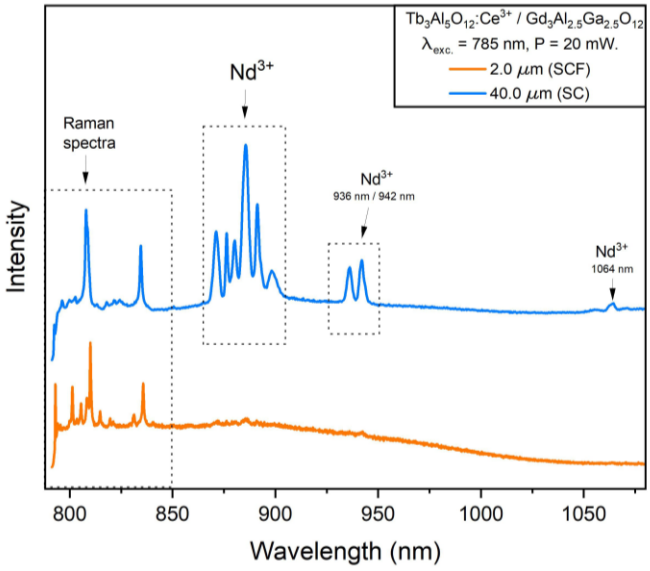
$m = \frac{a_{SCF} - a_{sub}}{a_{sub}} \times 100\%$ where a_{SCF} and a_{sub} are the stress-free lattice parameters of the film and substrate, respectively. The lattice misfit parameter (m) values for the TbAG:Ce SCFs grown onto the GAGG SC and YAG SC substrates are about -1.32 % and 0.53 %, respectively. Despite

relatively high lattice misfit parameter values, the TbAG:Ce SCF can be stably grown onto the YAG SC and GAGG SC substrates.[60] However, because of the differences in lattice constants, i.e. a smaller lattice constant of YAG (12.011 Å) and a larger lattice constant of GAGG (12.233 Å) with respect to the TbAG:Ce (12.073 Å), the epitaxial film will undergo a compressive and tensile epitaxial strain, respectively. This strain can influence: i) the replacement of Al^{3+} cations by Ga^{3+} cations in tetrahedral and octahedral coordination sites, ii) bond lengths within polyhedral structures, and iii) bond polarizability, where an increase in polarizability corresponds to higher band intensity in the spectra. Presumably, the occurrence of tensile epitaxial strain near and in the TL region caused by the difference in lattice constants between the TbAG:Ce SCF and GAGG SC substrate is the reason for the increase in band intensity at 464 cm^{-1}. The extinction of the band in the SC substrate is related to the relaxation of mechanical stress in its region where the crystal structure is much better ordered than in the TL, through the excitation of other lattice vibrations. The fact that we didn't observe such an effect for the YAG SC substrate is related to the possibility that there is a lower mechanical strain in the TL between the SCF and SC substrate because of a smaller lattice misfit parameter value or also because of the nature of the mechanical strain that occurs near the TL region, because as mentioned earlier, for YAG substrate it is a compressive strain, while for GAGG substrate it is tensile. Although Raman spectroscopy is a very useful method used in the study of stress in epitaxial structures, e.g. semiconductors (layers with nanometer thickness), in the case of study of single crystalline films (thickness from several to several dozen micrometers) it does not allow for obtaining direct and qualitative information on the stress occurring in the region of the transition layer around which the stress occurs.

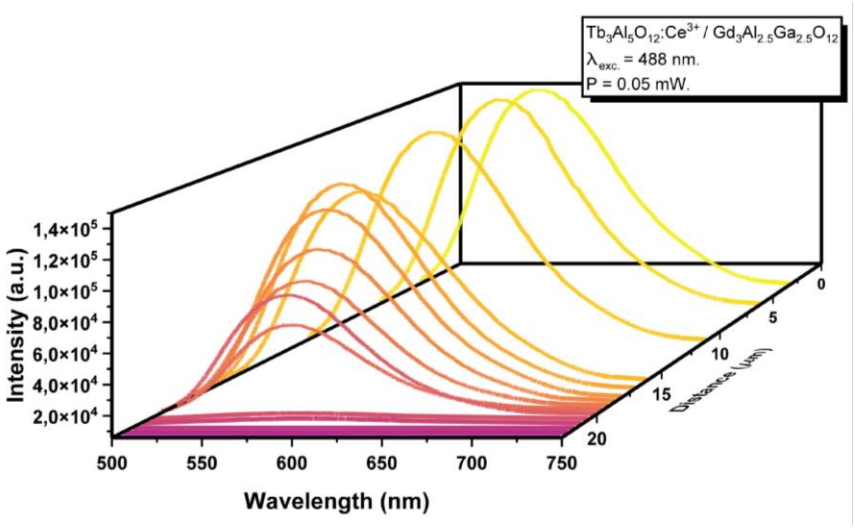
3.2 High spectral resolution luminescence

High-resolution luminescence spectra (HRLS) of $Tb_3Al_5O_{12}$:Ce SCFs grown onto

$Gd_3Al_{2.5}Ga_{2.5}O_{12}$ and $Y_3Al_5O_{12}$ SCs were recorded at RT using an x150 lens and two excitation wavelengths. The measurements were carried out using the 488 nm excitation line of an Ar^+ ion laser with an output power of 0.05 mW and the 785 nm excitation line of a semiconductor laser with an output power of 20 mW. The selected HRLS of the TbAG:Ce/GAGG structure probed from the SCF surface alongside the sample cross-section to the SC substrate surface under an excitation with 785 nm wavelength is shown in Figure 4a. A similar plot for the same sample, obtained under 488 nm excitation wavelength is provided in the supplementary information (Fig. S1). The three-dimensional plots shown in Figure 4b illustrate the obtained spectra as a function of probing distance under the 488 nm excitation wavelength. An analogous three-dimensional plot for the obtained HSRL spectra upon excitation with a 785 nm wavelength is included in the supplementary information in Figure S2.



(a)



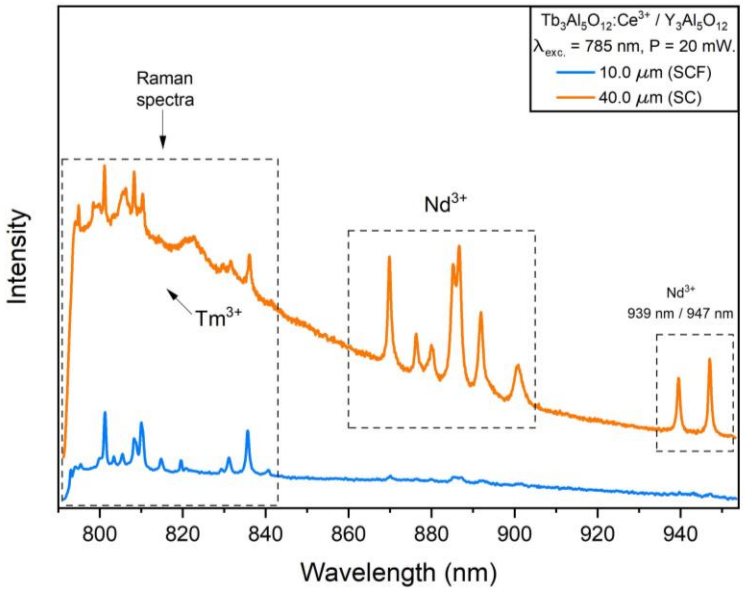
(b)

Figure 4. Selected HRLS of $Tb_3Al_5O_{12}$:Ce SCF/$Gd_3Al_{2.5}Ga_{2.5}O_{12}$ SC structure obtained under 785 nm excitation (a) and three-dimensional HRLS of $Tb_3Al_5O_{12}$:Ce SCF grown onto $Gd_3Al_{2.5}Ga_{2.5}O_{12}$ SC obtained under 488 nm excitation (b).

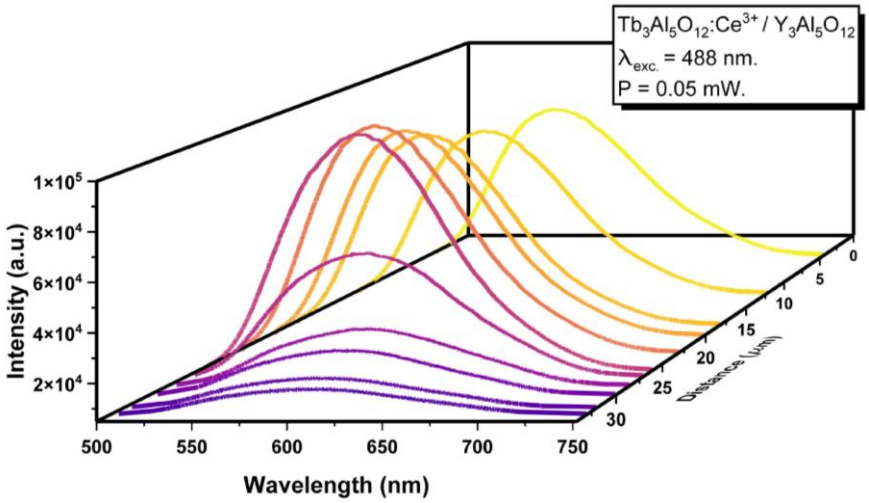
The recorded spectra under the 488 nm excitation line show a visible wide emission band composed of two overlapping broad bands, pertaining to two $5d^1 \rightarrow 4f^2$ electronic transitions of the Ce^{3+} ions - from the lowest level of the excited $5d^1$ state to the $^2F_{7/2}$ and $^2F_{5/2}$ sub-levels of the 4f ground state. The electronic configuration of Ce^{3+} is [Xe] $4f^1$, with one open-shell electron that can occupy different orbitals, resulting in possible degeneracies that can be uplifted by several interactions such as i) electron repulsion, ii) the Zeeman effect, iii) the Stark effect, iv) spin-orbit coupling and v) the influence of the crystal field of the host lattice. The primary contribution to the splitting of the 4f energy levels into $^2F_{7/2}$ and $^2F_{5/2}$ sub-levels derives from spin-orbit coupling.[63,64] The 5d excited state is highly sensitive to the surrounding crystal environment since it is less-shielded comparing to the 4f ground state. This means that external factors, such as the crystal field and local bonding interactions, have a stronger effect on the energy levels of 5d

electrons than on the 4f electrons which are more deeply embedded.[64] The consequence of this phenomenon is the splitting of the energy levels of the 5d excited state into two main sub-levels: $^2D_{5/2}$ and $^2D_{3/2}$. Higher-energy $^2D_{5/2}$ state electrons are unstable and tend to relax to the lower-energy $^2D_{3/2}$ state through interactions with lattice vibrations (electron-phonon coupling).[63] As a result, the Ce^{3+} emission band is asymmetric and corresponds to the $^2D_{3/2} \rightarrow {}^2F_{7/2}$ and $^2D_{3/2} \rightarrow {}^2F_{5/2}$ electronic transitions. The intensity of the Ce^{3+} emission reaches its maximum within the SCF and progressively diminishes in the substrate (Figs. 4b, S1). HRLS under excitation at the 785 nm (see Figs. 4a and S2) contain peaks that have been attributed to the emission lines of Nd^{3+} impurities. Their intensity is the highest in the GAGG SC substrate, which indicates its trace dopants to be the main source of contamination. Formally, it is important to compare spectra obtained from the same host material, as the luminescence of lanthanide elements can vary due to effects related to the host lattice, such as centroid shift and crystal field splitting. However, due to the lack of previous literature data in the context of HRLS for $Gd_3Al_{2.5}Ga_{2.5}O_{12}$ with a 785 nm excitation wavelength, the process of identifying unintentional impurities was done by comparing our previous studies on epitaxial SCFs of garnets grown onto on SC substrates.[44,47,53] The peaks that are visible in the range 869–900 nm, at 936 nm and 942 nm, and at around 1064 nm were assigned to $^4F_{3/2} \rightarrow {}^4I_{9/2}$ and $^4F_{3/2} \rightarrow {}^4I_{11/2}$ electronic transitions of Nd^{3+} ions. Due to the lack of presence of other unintentional dopants in the HRLS recorded with an excitation wavelength of 785 nm besides the identified Nd^{3+} ions, the three-dimensional plot (Fig. S2) was restricted to the 787-953 nm range. Similarly, selected HRLS for the TbAG:Ce/YAG sample obtained under the excitation at 785 nm and 488 nm are shown in Figures 5a and S3 (check supplementary information), respectively. Analogous three-dimensional plots illustrating the obtained HRLs as a function of probing distance are shown on Figure 5b and Figure S4 (which is provided in supplementary information) for excitation

wavelengths of 488 and 785 nm, respectively. The Ce^{3+} emission band obtained at 488 nm excitation behaves similarly to those of TbAG:Ce/GAGG, with the difference being the depth at which luminescence that is associated with $5d^1 \rightarrow 4f^2$ electronic transitions fades out.



(a)



(b)

Figure 5. (a) - Selected HRLS of $Tb_3Al_5O_{12}$:Ce/$Y_3Al_5O_{12}$ obtained under 785 nm excitation. (b) - three-dimensional HSRL spectra of $Tb_3Al_5O_{12}$:Ce SCF grown onto $Y_3Al_5O_{12}$:Ce SC obtained under 488 nm excitation.

In the spectra obtained by an excitation using a wavelength of 785 nm (Figs. 5a and S4), the recognized unintentional dopants observed were Tm^{3+} and Nd^{3+}. The intensity of the sharp bands and the background increases with distance, transitioning from the TbAG:Ce SCF to the YAG SC substrate. The broad bands located at around 800-840 nm were assigned to the $^3H_4 \rightarrow {}^3H_6$ electronic transitions of Tm^{3+} ions.[44] For the recognized Nd^{3+} ions, the same emission bands were observed as for the TbAG:Ce/GAGG sample and attributed to the previously described electronic transitions. Comparing the two Nd^{3+} emission bands in the 935-950 nm range (Figs. 4a, 5a), we observe that their position changes depending on the host substrate (GAGG/YAG) on which the epitaxial TbAG:Ce SCF was grown. For the GAGG SC substrate, we observe the above mentioned bands at 936 and 942 nm, while for the YAG SC substrate, the same bands appear at 939 nm and 947 nm. This is a consequence of the effect mentioned earlier, demonstrating that the luminescence of rare earth elements can vary due to effects related to the host lattice. The position of the Nd^{3+} emission bands for the YAG SC substrate is consistent with the results previously obtained by Dewo et al. for the same SC substrate.[44]

Figure 6 illustrates the areas of the Ce^{3+} $5d^1 \rightarrow 4f^2$ emission bands for the TbAG:Ce/GAGG and TbAG:Ce/ YAG samples as a function of measurement distance. Comparing the integral intensities of this bands, it is observable that for the TbAG:Ce SCFs grown onto the GAGG SC substrate, the intensities have subtly greater maximum values than for the YAG SC substrate, indicating a higher Ce^{3+} dopant content. It is seen that after passing through the TL zone, the observed emission band does not disappear abruptly but gradually lowers its integral intensity in the case of the sample for which the host material is $Gd_3Al_{2.5}Ga_{2.5}O_{12}$, to almost completely fade out while moving deeper into the substrate. In case of the sample with the $Y_3Al_5O_{12}$ substrate, a slight intensification of the emission band is observable after passing through the TL, but then it acts similarly to the GAGG

sample – almost completely fades out while moving deeper into the substrate area (Fig. 6). Former research describing the 5d-4f luminescence of the Ce^{3+} ions in YAG:Ce SCFs grown onto YAG and LuAG SC substrates also showed that the Ce^{3+} emission band does not instantly vanish at depths greater than TL region.[47] To elucidate this effect, it is essential to understand the LPE growth process of SCFs onto SC substrates.

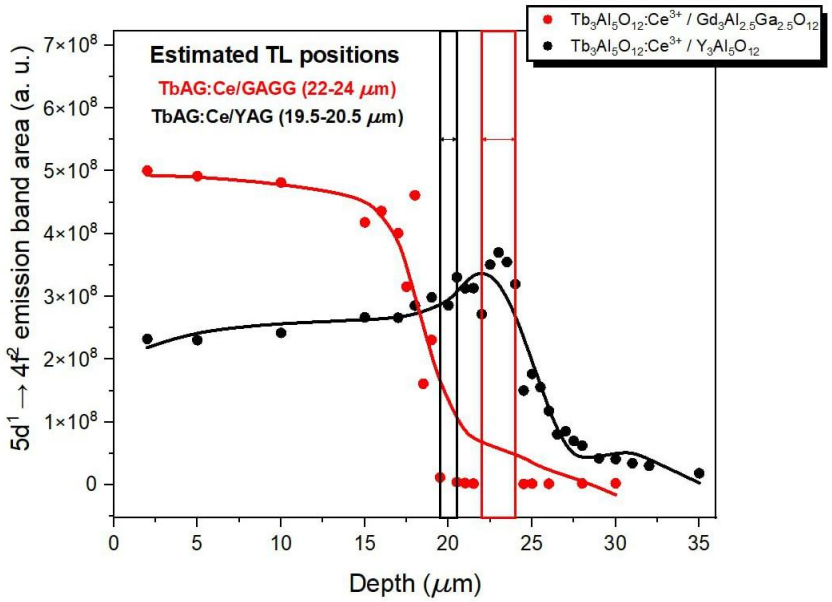


Figure 6. The Ce^{3+} $5d^1 \rightarrow 4f^2$ emission band area as a function of probing distance for TbAG:Ce^{3+}/GAGG and TbAG:Ce^{3+}/YAG structures. The estimated positions and thicknesses of the TL are illustrated with red and black rectangles for TbAG:Ce/GAGG and TbAG:Ce/YAG structures, respectively.

To grow TbAG:Ce SCFs onto GAGG and YAG substrates via LPE method, fluxes such as PbO–B_2O_3 are employed to lower the melting point of the deposited material. This enables quasi-homoepitaxial growth of the SCF on the substrate while simultaneously preventing significant over-melting of the substrate. However, in practice, some over-melting does occur, though its extent is limited to the nanometer scale. Therefore, the slight intensification of the Ce^{3+}emission

band in the TL region cannot be attributed to the diffusion of cerium ions from the melt into the substrate as a consequence of substrate over-melting during the quasi-homoepitaxial growth process. To disqualify the possibility of diffusion of cerium ions into the substrate area, the asymmetry ratio R was defined as: $R = \frac{I_2}{I_1}$ where $I_2 = I(^2D_{3/2} \rightarrow {}^2F_{7/2})$ and $I_1 = I(^2D_{3/2} \rightarrow {}^2F_{5/2})$ are the integral intensities of the Ce^{3+} emission bands corresponding to the relevant electronic transitions. The asymmetry ratio R indicates how the surrounding crystal field affects the luminescence properties of the Ce^{3+} ions. In the scientific literature on garnet crystals, the concept of asymmetry ratio was used to analyze the luminescent properties of Eu^{3+} ions in $Gd_3Al_{2.5}Ga_{2.5}O_{12}$ garnets by Głuchowski et al..[62] To compare the influence of the host lattice on Ce^{3+} luminescence, the obtained data on HRLS for $Tb_3Al_5O_{12}$:Ce/$Y_3Al_5O_{12}$ and for $Y_3Al_5O_{12}$:Ce/$Y_3Al_5O_{12}$ structures from our previous studies were used.[47] The emission bands were fitted using a mixed Gaussian/Lorentzian function, and then the asymmetry ratio was calculated for the TbAG:Ce and YAG:Ce samples and shown as a function of probing distance in Figure 7.

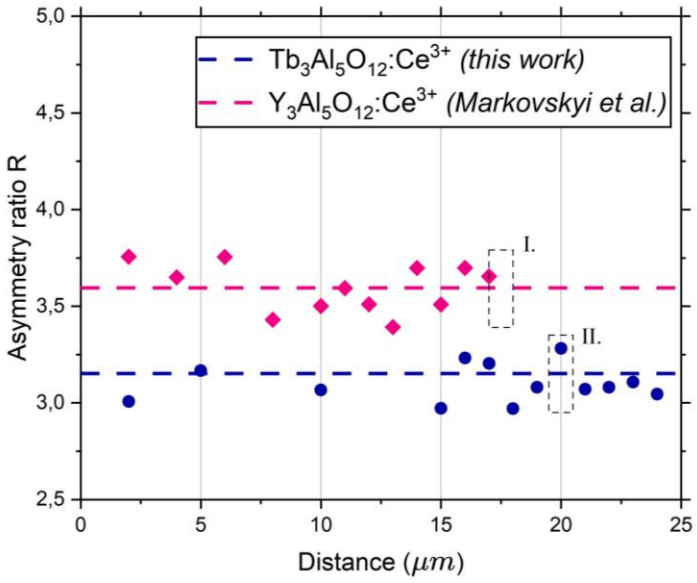


Figure 7. Values of R asymmetry ratio measured for $Tb_3Al_5O_{12}$:Ce and $Y_3Al_5O_{12}$:Ce SCFs as a function of probing distance. Marked areas I and II correspond to the TL positions estimated by

Raman measurements for $Y_3Al_5O_{12}$:Ce/$Y_3Al_5O_{12}$ structure (Markovskyi et. al) and $Tb_3Al_5O_{12}$:Ce/$Y_3Al_5O_{12}$ structure (this work), respectively.

Regardless of cross-section depth, the asymmetry ratio value fluctuates around 3.15 for $Tb_3Al_5O_{12}$:Ce SCF. In case of $Y_3Al_5O_{12}$:Ce its value is approximately 3.59. Relatively similar values of asymmetry ratio for these two samples are mainly a result of the structural similarity of TbAG and YAG garnets. If a hypothetical migration of cerium ions into the YAG substrate were to occur, an increase in the value of the parameter R to about 3.6 should be observed. That means there is no evidence of possible migration of cerium ions deep into the substrate area. In case of the TbAG:Ce/GAGG structure, it was concluded that the observed luminescence signal in the substrate area is a result of the same reason as for the TbAG:Ce/YAG structure. One of the possible explanations for the Ce^{3+} luminescence still observed in the substrate could be related to the optical system of the microscope. Even though the microscope is confocal, the spatial and depth resolution is diffraction limited. Thus, when we record the luminescence spectra close to TL (a few micrometers far) the laser light still excites the Ce^{3+} ions in the SCF and the optics (lens) still collects Ce^{3+} emission.

4. Conclusions

Raman and high-resolution luminescence spectroscopy studies were performed on Ce^{3+} - doped $Tb_3Al_5O_{12}$ (TbAG:Ce) single crystalline films (SCFs) grown onto $Y_3Al_5O_{12}$ (YAG) and $Gd_3Al_{2.5}Ga_{2.5}O_{12}$ (GAGG) single crystal substrates using the liquid phase epitaxy (LPE) method in so called quasi-homoepitaxial growth mode. The measured lattice mismatch between the TbAG:Ce SCF and the YAG and GAGG substrates was 0.53% and –1.32%, respectively. Due to the differences in lattice constants of YAG (12.011 Å) and a larger lattice constant of GAGG (12.233 Å) with respect to the TbAG:Ce (12.073Å), the TbAG:Ce SCF will undergo a compressive

and tensile epitaxial strain, respectively. This indicates also that the TbAG:Ce SCF grown on the GAGG substrate experiences a greater and negative residual stress compared to the SCF grown on the YAG substrate. All experimentally observed Raman modes of the TbAG:Ce SCFs and substrates were classified and assigned. Raman spectra collected from the cross-sections of both samples revealed the spectral evolution from the SCF/substrate interface through the transition layer to the substrate. Shifts in the positions of Raman modes for the two epitaxial structures are consistent with above mentioned changes in lattice constants between the SCF and the substrate.

High-resolution luminescence spectra recorded under 488 nm excitation show the characteristic 5d–4f emission of Ce^{3+} ions. In contrast, excitation in the near-infrared region at 785 nm reveals 4f–4f emissions from trace impurities. Interestingly, residual Ce^{3+} emission is still detected in the YAG substrate, which is nominally undoped with Ce^{3+}. To investigate this, we calculated the asymmetry ratio (R) for the TbAG:Ce SCF/ $Y_3Al_5O_{12}$ epitaxial structure and compared it with values obtained in our previous study for a $Y_3Al_5O_{12}$:Ce SCF/YAG structure. The calculated R values for these structures differ by more than 12%. Moreover, in the case of the TbAG:Ce SCF/YAG structure, the R value remains constant even when moving into the YAG substrate region. A more plausible explanation for the "observed" Ce^{3+} luminescence in the YAG substrate involves limitations of the optical system. Although the microscope used is confocal, its spatial and depth resolution is diffraction-limited. Consequently, when luminescence spectra are recorded near the transition layer (just a few micrometers into the substrate) the excitation laser may still reach Ce^{3+} ions in the SCF, and the collection optics may still detect their emission.

The obtained results provide a deeper understanding of the structural and optical properties of garnet SCFs grown via quasi-homoepitaxial mode. Furthermore, the investigation of freshly fractured cross-sections of Ce^{3+} - doped $Tb_3Al_5O_{12}$ SCFs grown on $Y_3Al_5O_{12}$ and $Gd_3Al_{2.5}Ga_{2.5}O_{12}$

single crystal substrates enables the measurement of Raman and high-resolution luminescence spectra with maximal spatial resolution.

Data availability

The authors affirm that the data supporting the conclusions of this study are presented in the article and its supplementary information. Additional raw data are available from the corresponding author, upon reasonable request.

Supplementary information

Supplementary information for this article can be found in the appendix.

Corresponding Author

*Tomasz Runka; Email: tomasz.runka@put.poznan.pl

*Yurii Syrotych; Email: syr@ukw.edu.pl

Author Contributions

Yurii Syrotych – Conceptualization, Investigation, Data curation, Writing – original draft.

Maciej Rzeczkowski - Investigation, Data curation, Writing – original draft.

Piotr Radomski – Investigation.

Vitaliy Gorbenko – Investigation.

Yuriy Zorenko – Conceptualization, Supervision, Writing – review & editing.

Tomasz Runka – Conceptualization, Supervision, Writing – original draft, Writing – review & editing.

Conflict of interest

The authors declare no conflict of interest.

Acknowledgements

This work was performed in the frame of the research project of the Ministry of Science and High Education (T.R., M.Rz., P.R.) research project of National Scientific Centre (NCN) Opus 23 project No OPUS 2022/45/B/ST8/01757 (Y.Z., V.G., Y.S.) and also supported by the Ministry of Science and High Education of Poland in frame of Regional Excellence Initiative nr RID/SP/ 0048/2024/01 project (Y.S.).

References

1. M. Nikl and A. Yoshikawa, Recent R&D Trends in Inorganic Single-Crystal Scintillator Materials for Radiation Detection, *Adv. Opt. Mater.*, 2015, **3**, 463–481.

2. Z. Xia and Q. Liu, Progress in discovery and structural design of color conversion phosphors for LEDs, *Prog. Mater. Sci.*, 2016, **84**, 59–117.

3. M. Nikl, A. Yoshikawa, K. Kamada, K. Nejezchleb, C.R. Stanek, J.A. Mares and K. Blazek, Development of LuAG-based scintillator crystals – A review, *Prog. Cryst. Growth Charact. Mater.,* 2013, **59**, 47–72.

4. C. Dujardin, E. Auffray, E. Bourret-Courchesne, P. Dorenbos, P. Lecoq, M. Nikl, A.N. Vasil'ev, A. Yoshikawa and R.-Y. Zhu, Needs, Trends, and Advances in Inorganic Scintillators, *IEEE Trans. Nucl. Sci.*, 2018, **65**, 1977–1997.

5. Z. Xia and A. Meijerink, Ce^{3+}-Doped garnet phosphors: composition modification, luminescence properties and applications, *Chem. Soc. Rev.*, 2017, **46**, 275–299.

6. J. Bi, J.G. Li, Q. Zhu, J.Chen, X. Li, X. Sun, B.N. Kim and Y. Sakka, Yellow-Emitting $(Tb_{1-x}Ce_x)_3Al_5O_{12}$ Phosphor Powder and Ceramic ($0 \leq x \leq 0.05$): Phase Evolution, Photoluminescence, and the Process of Energy Transfer, *Ceram. Int.*, 2017, **43**, 8163–8170.

7. J.G. Li and Y. Sakka, Recent progress in advanced optical materials based on gadolinium aluminate garnet ($Gd_3Al_5O_{12}$), *Sci. Technol. Adv. Mater.*, 2015, **16**, 014902.

8. G. Li, Y. Tian, Y. Zhao and J. Lin, Recent progress in luminescence tuning of Ce^{3+} and Eu^{2+}-activated phosphors for pc-WLEDs, *Chem. Soc. Rev.*, 2015, **44**, 8688–8713.

9. K. Bando, K. Sakano, Y. Noguchi and Y. Shimizu, Development of High-bright and Pure-white LED Lamps, *J Light Visual Environ.*, 1998, **22**, 2–5.

10. M.R. Krames, O.B. Shchekin, R. Mueller-Mach, G.O. Mueller, L. Zhou, G. Harbers and M.G. Craford, Status and Future of High-Power Light-Emitting Diodes for Solid-State Lighting, *J. Disp. Technol.*, 2007, **3**, 160–175.

11. P. Schlotter, J. Baur, C. Hielscher, M. Kunzer, H. Obloh, R. Schmidt and J. Schneider, Fabrication and characterization of GaN/InGaN/AlGaN double heterostructure LEDs and their application in luminescence conversion LEDs. *J. Mater. Sci. Eng. B*, 1999, **59**, 390–394.

12. Y. Chen, M. Gong, G. Wang and Q. Su, High efficient and low color-temperature white light-emitting diodes with $Tb_3Al_5O_{12}$:Ce^{3+} phosphor. *Appl. Phys. Lett.*, 2007, **91**, 071117.

13. P. Bolek, J. Zeler, V. Gorbenko, T. Zorenko, P. Popielarski, K. Bartosiewicz, A. Osvet, M. Batentschuk, E. Zych and Y. Zorenko, Luminescent Properties of Nanopowder and Single-Crystalline Films of TbAG:Ce Garnet, *Phys. Status Solidi B*, 2020, **257**, 1900495.

14. J. Chen, Y. Tang, X. Yi, Y. Tian, G. Ao, D. Hao, Y. Lin and Z. Shengming, Fabrication of $(Tb,Gd)_3Al_5O_{12}:Ce^{3+}$ phosphor ceramics for warm white light-emitting diodes application, *Opt. Mater. Express*, 2019, **9**, 3333-3341.

15. M. Batentschuk, A. Osvet, G. Schierning, A. Klier, J. Schneider and A. Winnacker, Simultaneous excitation of Ce^{3+} and Eu^{3+} ions in $Tb_3Al_5O_{12}$, *Radiat. Meas.*, 2004, **38**, 539–543.

16. R. Turos-Matysiak, W. Gryk, M. Grinberg, Y.S. Lin and R.S. Liu, $Tb^{3+}\rightarrow Ce^{3+}$ energy transfer in $Y_{3-x-y}Tb_yGd_xAl_5O_{12}$ (x=0.65, y=0.575) doped with Ce^{3+}, *Radiat. Meas.*, 2007, **42**, 755–758.

17. K. Bartosiewicz, V. Babin, M. Nikl, J.A. Mares, Y. Zorenko and V. Gorbenko, Luminescence and energy transfer processes in $(Lu,Tb)_3Al_5O_{12}$ single crystalline films doped with Ce^{3+}, *J.Lumin.*, 2016, **173**, 141–148.

18. A.A. Setlur, J.J. Shiang and C.J. Vess, Transition from Long-Range to Short-Range Energy Transfer through Donor Migration in Garnet Hosts, *J. Phys. Chem. C*, 2011, **115**, 3475–3480.

19. Y. Zorenko, T. Voznyak, V. Vistovsky, T. Zorenko, S. Nedilko, M. Batentschuk, A. Osvet, A. Winnacker, G. Zimmerer, V. Kolobanov and D. Spassky, Energy transfer to Ce^{3+} ions in $Tb_3Al_5O_{12}$:Ce single crystalline films. *Radiat. Meas.*, 2007, **42**, 648–651.

20. D. Kundaliya, M. Raukas, A.M. Scotch, D. Hamby, K. Mishra and M. Stough, Wavelength Converter for an LED and LED Containing Same, US Pat., 8,937,332 B2, 2015.

21. A. Markovskyi, V. Gorbenko, T. Yokosawa, J. Will, E. Spiecker, M. Batentschuk, J. Elia, A. Fedorov, M. Pakuła, M. Kaczmarek and Y. Zorenko, Structural, luminescence and photoconversion properties of $Lu_3Al_5O_{12}$:Ce single crystalline film phosphors for WLED application, *J. Alloys Compd.,* 2022, **929**, 167159.

22. A. Markovskyi, V. Gorbenko, T. Zorenko, A. Fedorov and Y. Zorenko, Color converters for white LEDs using liquid phase epitaxy growth method, *J.Lumin.*, 2024, **266**, 120313.

23. Y. Zorenko, M. Batentschuk, C. Brabec, A. Osvet, V. Gorbenko, I. Levchuk, T. Zorenko, L. Chepyga, A. Markovskyi and S. Witkiewicz-Lukaszek. Composite wavelength converter. EU EP 3831911A1, 2021.

24. A. Markovskyi, V. Gorbenko, Y. Zorenko, K. Bartosiewicz and A. Fedorov, Development of $Tb_{1.5}Gd_{1.5}Al_5O_{12}$:Ce Single-Crystalline Film Converters for WLED Using a Liquid Phase Epitaxy Growth Method. *Crystals*, 2022, **12**, 1814.

25. A. Markovskyi, V. Gorbenko, T. Zorenko, S. Nizhankovskiy, A. Fedorov and Y. Zorenko, Composite color converters based on $Tb_3Al_5O_{12}$:Ce single crystalline films and $Y_3Al_5O_{12}$:Ce crystal substrates, Phys. Status Solidi RRL, 2021, **15**, 2100173.

26. A. Markovskyi, V. Gorbenko, S. Nizhankovskiy, T. Zorenko, M. Pakuła, M. Kaczmarek, A. Fedorov and Y. Zorenko, Novel composite color converters based on $Tb_{1.5}Gd_{1.5}Al_5O_{12}$:Ce single crystalline films and $Y_3Al_5O_{12}$:Ce crystal substrates. CrystEngComm, 2022, **27**, 4975-4982.

27. A. Markovskyi, V. Gorbenko, T. Zorenko, S. Witkiewicz-Lukaszek, O. Sidletskiy, A. Fedorov and Y. Zorenko, Development of Three-Layered Composite Color Converters for White LEDs Based on the Epitaxial Structures of YAG:Ce, TbAG:Ce and LuAG:Ce Garnets. *Materials*, 2023, **16**, 1848.

28. S. V. Nizhankovskyi, A.V. Tan'ko, Y.N. Savvin, S.I. Krivonogov, A.T. Budnikov and A.V. Voloshin, Single crystalline YAG:Ce phosphor for powerful solid-state sources of white light. The influence of production conditions on luminescence properties and lighting characteristics, *Opt. Spectrosc.*, 2016, **120**, 915–921.

29. S. Ganschow, D. Klimm, P. Reiche and R. Uecker, On the Crystallization of Terbium Aluminium Garnet, *Cryst. Res. Technol.*, 1999, **34**, 615–619.

30. V.I. Chani, A. Yoshikawa, H. Machida and T. Fukuda, $(Tb, Yb)_3Al_5O_{12}$ garnet: crystal-chemistry and fiber growth by micro-pulling-down technique, *J. Mater. Sci. Eng. B*, 2000, **75**, 53–60.

31. V.I. Chani, A. Yoshikawa, H. Machida and T. Fukuda, Melt growth of $(Tb,Lu)_3Al_5O_{12}$ mixed garnet fiber crystals, *J. Cryst. Growth*, 2000, **212**, 469–475.

32. Y. Zorenko and V. Gorbenko, Growth peculiarities of the $R_3Al_5O_{12}$ (R= Lu, Yb, Tb, Eu-Y) single crystalline film phosphors by Liquid Phase Epitaxy, *Rad. Meas.*, 2007, **42**, 907-910.

33. Y. Zorenko, V. Gorbenko, T. Voznyak, T. Zorenko, B. Kuklinski, R. Turos-Matysyak and M. Grinberg, Luminescence properties of phosphors based on $Tb_3Al_5O_{12}$ (TbAG) terbium-aluminum garnet. *Opt. Spectrosc.*, 2009, **106**, 365–374.

34. M.A. Haque, Z.H. Mahmood and J. Rahman, Liquid Phase Epitaxy for Optical Communication Devices, *Bangladesh J. Sci. Ind. Res.*, 2009, **44**, 297-302.

35. J.M. Robertson, W. Tolksdorf and H.D. Jonker, Growth mechanisms and composition in the LPE process for bubble domain materials, *J. Cryst. Growth*, 1974, **27**, 241-248.

36. B. Ferrand, B. Chambaz and M. Couchaud, Liquid phase epitaxy: A versatile technique for the development of miniature optical components in single crystal dielectric media, *Opt. Mater.*, 1999, **11**, 101-114.

37. P. Capper and M. Mauk, Liquid Phase Epitaxy of Electronic, Optical and Optoelectronic Materials, John Wiley & Sons, Ltd, 2007.

38. Y. Zorenko, P.A. Douissard, T. Martin, F. Riva, V. Gorbenko, T. Zorenko, K. Paprocki, K. Iskalieva, S. Witkiewicz, A. Fedorov, P. Bilski and A. Twardak, Scintillating screens based on the LPE grown $Tb_3Al_5O_{12}$:Ce single crystalline films, *Opt.Mater.*, 2017, **65**, 73–81.

39. S. Witkiewicz-Lukaszek, V. Gorbenko, T. Zorenko, O. Sidletskiy, P. Arhipov, A. Fedorov, J.A. Mares, R. Kucerkova, M. Nikl and Y. Zorenko, Liquid phase epitaxy growth of high-performance composite scintillators based on single crystalline films and crystals of LuAG, *CrystEngComm*, 2020, **22**, 3713–3724.

40. S. Witkiewicz-Lukaszek, V. Gorbenko, T. Zorenko, Y. Syrotych, J.A. Mares, M. Nikl, O. Sidletskiy, P. Bilski, A. Yoshikawa and Y. Zorenko, Composite detectors based on single crystalline films and single crystals of garnet compounds, *Materials*, 2022, **15**, 1249.

41. G. Menzer, Die Kristallstruktur der Granate, *Z. Kristallogr. - Cryst. Mater.*, 1929, **69**, 300–396.

42. R.D. Shannon, Revised Effective Ionic Radii and Systematic Studies of Interatomic Distances in Halides and Chalcogenides, *Acta Cryst. A*, 1976, **32**, 751–767.

43. Y.-C. Lin, M. Bettinelli and M. Karlsson, Unraveling the Mechanisms of Thermal Quenching of Luminescence in Ce^{3+}- Doped Garnet Phosphors, *Chem. Mater.*, 2019, **31**, 3851–3862.

44. W. Dewo, V. Gorbenko, A. Markovskyi, Y. Zorenko and T. Runka, Photoconversion, Luminescence and Vibrational Properties of Mn and Mn,Ce Doped $Tb_3Al_5O_{12}$ Garnet Single Crystalline Films, *J. Lumin.*, 2023, **254**, 119481.

45. K. Papagelis and S. Ves, Vibrational Properties of the Rare Earth Aluminum Garnets, *J. Appl. Phys.*, 2003, **94**, 6491–6498.

46. K. Papagelis, G. Kanellis, J. Arvanitidis, G.A. Kourouklis and S. Ves, Phonons in Rare-Earth Aluminum Garnets and Their Relation to Lattice Vibration of AlO_4., *Phys. Status Solidi B*, 1999, **215**, 193–198.

47. A. Markovskyi, P. Radomski, W. Dewo, V. Gorbenko, A. Fedorov, T. Runka and Y. Zorenko, Photoluminescence and Raman Spectroscopy of Ce^{3+} Doped $Y_3Al_5O_{12}$ Single Crystalline Films Grown onto $Y_3Al_5O_{12}$ and $Lu_3Al_5O_{12}$ Substrates, *Mater. Res. Bull.*, 2025, **182**, 113141.

48. K. Papagelis and S. Ves, Infrared Spectroscopy and Lattice Dynamical Calculations of $Gd_3Al_5O_{12}$, $Tb_3Al_5O_{12}$ and $Lu_3Al_5O_{12}$ Single Crystals, *J. Phys. Chem. Solids*, 2003, **64**, 599–605.

49. G. Mace, G. Schaack, N. Toaning and J.A. Koningstein, Optical Phonons of Terbium, Dysprosium and Ytterbium Garnet, *Z. Phys.*, 1970, **230**, 391–402.

50. K. Papagelis, G. Kanellis, S. Ves and G.A. Kourouklis, Lattice Dynamical Properties of the Rare Earth Aluminum Garnets ($RE_3Al_5O_{12}$), *Phys. Status Solidi B*, 2002, **233**, 134–150.

51. J. Arvanitidis, K. Papagelis, D. Christofilos, H. Kimura, G.A. Kourouklis and S. Ves, High Pressure Raman Study of $Y_3Al_5O_{12}$, *Phys. Status Solidi B*, 2004, **241**, 3149–3154.

52. K. Papagelis, J. Arvanitidis, G. Kanellis, S. Ves and G.A. Kourouklis, Effect of High Hydrostatic Pressure on the Phonon Modes of $Tb_3Al_5O_{12}$ and $Dy_3Al_5O_{12}$ Single Crystals, *Phys. B*, 1999, **265**, 277–281.

53. W. Dewo, V. Gorbenko, Y. Zorenko and T. Runka, Raman Spectroscopy of Ce^{3+}-Doped $Lu_3Al_5O_{12}$ Single Crystalline Films Grown onto $Y_3Al_5O_{12}$ Substrate, *Opt. Mater.:X*, 2019, **3**, 100029.

54. A. Markovskyi, V. Gorbenko, T. Zorenko, T. Yokosawa, J. Will, E. Spiecker, M. Batentschuk, J. Elia, A. Fedorov and Y. Zorenko, LPE Growth of $Tb_3Al_5O_{12}$:Ce Single Crystalline Film Converters for WLED Application, *CrystEngComm*, 2021, **23**, 3212–3219.

55. W. Dewo, V. Gorbenko, Y. Syrotych, Y. Zorenko and T. Runka, Mn-Doped $XAlO_3$ (X = Y, Tb) Single-Crystalline Films Grown onto $YAlO_3$ Substrates: Raman Spectroscopy Study toward Visualization of Mechanical Stress, *J. Phys. Chem. C*, 2021, **125**, 16279–16288.

56. K. Papagelis, J. Arvanitidis, E. Vinga, D. Christofilos, G.A. Kourouklis, H. Kimura and S. Ves, Vibrational Properties of $(Gd_{1-x}Y_x)_3Ga_5O_{12}$ Solid Solutions, *J. Appl. Phys.*, 2010, **107**, 113504.

57. K. Papagelis, J. Arvanitidis, G. Kanellis, S. Ves and G.A. Kourouklis, High-Pressure Effects on the Raman Spectrum and the Force Constants of the Rare-Earth Aluminium Garnets ($RE_3Al_5O_{12}$), *J. Phys.: Condens. Matter*, 2002, **14**, 3875-3890.

58. K. Papagelis, J. Arvanitidis, S. Ves and G.A. Kourouklis, Pressure Evolution of the Phonon Modes and Force Constants of $Tb_3Al_5O_{12}$ and $Lu_3Al_5O_{12}$, *Phys. Status Solidi B*, 2003, **235**, 348–353.

59. M. Poulos, S. Giaremis, J. Kioseoglou, J. Arvanitidis, D. Christofilos, S. Ves, M.P. Hehlen, N.L. Allan, C.E. Mohn and K. Papagelis, Lattice Dynamics and Thermodynamic Properties of $Y_3Al_5O_{12}$ (YAG), *J. Phys. Chem. Solids*, 2022, **162**, 110512.

60. Y. Syrotych, V. Gorbenko, S. Witkiewicz-Lukaszek, T. Zorenko, M. Kaczmarek, J. Pejchal, J.A. Mares, R. Kucerkova, M. Nikl, K. Kamada, A. Yoshikawa and Y. Zorenko, Scintillation Properties of Multilayered Composite Scintillators Based on the YAG:Ce and TbAG:Ce Single Crystalline Films and GAGG:Ce Crystal Substrates, *Opt. Mater.:X*, 2024, **24**, 100372.

61. V. Gorbenko, T. Zorenko, S. Witkiewicz, K. Paprocki, O. Sidletskiy, A. Fedorov, P. Bilski, A. Twardak and Y. Zorenko, LPE Growth of Single Crystalline Film Scintillators Based on Ce^{3+} Doped $Tb_{3-x}Gd_xAl_{5-y}Ga_yO_{12}$ Mixed Garnets, *Crystals*, 2017, **7**, 262.

62. P. Głuchowski, M. Małecka, W. Stręk, W. Ryba-Romanowski and P. Solarz, Size Effect in Novel Red Efficient Garnet Nanophosphor, *J. Phys. Chem. C*, 2017, **121**, 25561–25567.

63. J. Hasani Barbaran, M. Sasani Ghamsari, I. Javaheri and B. Baharvand, Growth and Spectral Properties of Ce^{3+}:YAG Single Crystal, *J. Optoelectron. Adv. Mater.*, 2018, **20**, 431–434.

64. N.I. Binti Mohd Razip, M. Novita and K. Ogasawara, Two-Step Model for Predicting 4f→5d Transition Energies of Ce^{3+} in Garnet-Type Oxides Based on First-Principles Calculations and Machine Learning, *Opt. Mater.*, 2025, **159**, 116653.